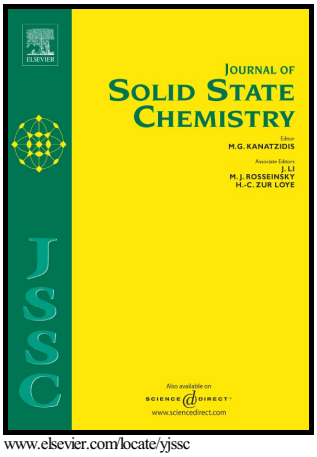

www.elsevier.com/locate/yjssc

Investigation of $Co_6(OH)_3(TeO_3)_4(OH)\sim0.9(H_20)$: Synthesis, crystal and magnetic structures, magnetic and dielectric properties

Morgane Poupon, Nicolas Barrier, Alain Pautrat, Sébastien Petit, Olivier Perez, Philippe Bazin

PII: S0022-4596(18)30495-X
DOI: https://doi.org/10.1016/j.jssc.2018.11.007
Reference: YJSSC20463

To appear in: *Journal of Solid State Chemistry*

Received date: 18 September 2018
Revised date: 5 November 2018
Accepted date: 7 November 2018

Cite this article as: Morgane Poupon, Nicolas Barrier, Alain Pautrat, Sébastien Petit, Olivier Perez and Philippe Bazin, Investigation of $Co_6(OH)_3(TeO_3)_4(OH)\sim0.9(H_20)$: Synthesis, crystal and magnetic structures, magnetic and dielectric properties, *Journal of Solid State Chemistry,* https://doi.org/10.1016/j.jssc.2018.11.007

Investigation of $Co_6(OH)_3(TeO_3)_4(OH)\sim0.9(H_20)$: Synthesis, crystal and magnetic structures, magnetic and dielectric properties

Morgane Poupon[a], Nicolas Barrier[a*], Alain Pautrat[a], Sébastien Petit[a], Olivier Perez[a], Philippe Bazin[b]

a. Laboratoire CRISMAT, Normandie Univ, ENSICAEN, UNICAEN, CNRS, 6 bd Maréchal Juin 14050 CAEN Cedex 4, France.

b. Laboratoire Catalyse & Spectrochimie, Normandie Univ, ENSICAEN, UNICAEN, CNRS, 6 bd Maréchal Juin 14050 CAEN Cedex 4, France.

* Corresponding Author

ABSTRACT

We have re-investigated the synthesis and the crystal structure of the non-centrosymmetric phase $Co_6(OH)_3(TeO_3)_4(OH)$ published by Perez *et al*. in 1975 and we have obtained by hydrothermal synthesis the hydrated phase $Co_6(OH)_3(TeO_3)_4(OH)\sim0.9(H_20)$. The crystal structure related to the Ellenbergerite mineral was determined using single-crystal X-ray diffraction data. The non-centrosymmetric hexagonal structure ($P6_3mc$; a = 13.1640(7) Å; c = 5.0321(6) Å) is based on [CoO_6] octahedra and [TeO_3] polyhedra which formed a tunnel framework with a formal charge 1+ balanced by one OH^- group located in large tunnels. Compared to $Co_6(OH)_3(TeO_3)_4(OH)$ case we succeeded in locating the hydrogen atoms of the OH^- groups bound to the Co and showed that a small amount of water resides also in the large tunnels with the OH^- groups. The presence of water molecules was confirmed by infrared spectroscopy and thermogravimetric analyses. This phase behaves as a canted antiferromagnet below T_N = 75.5 K. The average magnetic structure was solved from powder neutron

diffraction. Antisymmetric Dzyaloshinsky-Moriya interactions in the (ab) plane have been highlighted and must be responsible for the spin canted antiferromagnetic ground state. Moreover, DFT calculations with an Ising model show the presence of a frustrated spin state for the two Co^{2+} cations involved in the antisymmetric Dzyaloshinsky-Moriya interaction. Under an applied magnetic field, a metamagnetic-like behaviour is observed with three different canted antiferromagnetic states. At low temperature, dielectric measurements evidence a magneto-structural coupling but no measurable magnetocapacitance.

Graphical abstract:

$Co_6(OH)_3(TeO_3)_4(OH)$~0.9(H_20) was obtained by hydrothermal synthesis and its hexagonal non-centrosymmetric structure ($P6_3mc$) is related to the Ellenbergerite-like structure. Powder neutron diffraction experiments and DFT calculations revealed the presence of antisymmetric Dzyaloshinsky-Moriya interactions with frustrated spin state, the origin for the spin canted antiferromagnetic state. Metamagnetic-like behavior is also observed under applied magnetic field and three canted antiferromagnetic states can be distinguished. At low temperature, dielectric measurements evidence a magneto-structural coupling but no magnetocapacitance.

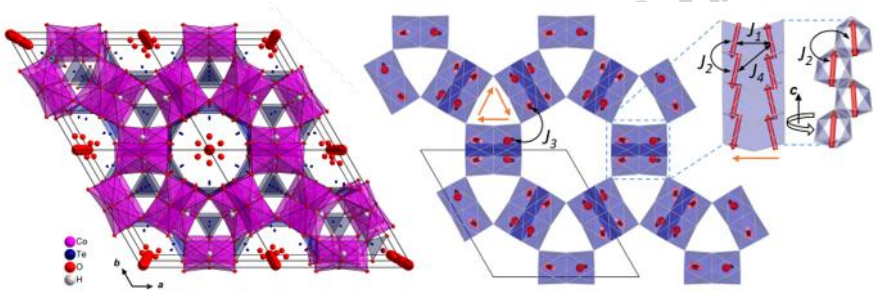

Keywords:

Hydrothermal synthesis; crystal structure; magnetic structure; magnetic properties; dielectric properties

1 INTRODUCTION

The study of materials with non-centrosymmetric structure is of interest regarding their numerous potential physical properties such nonlinear optic, piezoelectricity, pyroelectricity

and ferroelectricity.[1] Moreover, such structures coupled with magnetic cations may present multiferroic properties. To favour the synthesis of compounds with non-centrosymmetric structure, elements with stereochemically active lone pair such as Pb^{II}, Sn^{II}, Sb^{III}, Bi^{III}, Se^{IV}, Te^{IV} and I^{V} are commonly used due to the second order Jahn Teller (SOJT) distortions they generate in their respective coordination environments.[2] Among the oxotellurate(IV) compounds based on magnetic cations listed in the literature, $Co_6(OH)_3(TeO_3)_4(OH)$ published by Perez *et al*.[3] may be interesting for its non-centrosymmetric and polar hexagonal tunnel structure. This phase obtained by hydrothermal synthesis at high pressure (900 bar) and high temperature (380°C) belongs to a large family of Co-phases such as Co-vanadate $Co_6(OH)_2(H_2O)[VO_4]_4$,[4] Co-arsenate $Co_{1-x}Co_6(OH)_3[HAsO_4][H_{2x/3}AsO_4]_3$,[5] Co-phosphate $Co_{5.5}(OH)_3[HPO_3][HPO_3]_3$,[6] $Na_{2-x}Co_6(OH)_3[HPO_4][H_{x/3}PO_4]_3$ ($x \approx 1.1$)[7] and Co-selenate $Co_6(OH)_3(SeO_3)_4(OH)$.[8] All these phases present structural topologies similar to the aluminosilicate mineral Ellenbergerite $(Mg,Ti)Mg3(Mg,Al)_3(OH)_3[HSiO_4][H_{0.33}SiO_4]_3$.[9] The magnetic properties reported for the Co-vanadate, arsenate and phosphate phases show similar canted antiferromagnetic states below the magnetic temperature ordering. Nevertheless, no magnetic properties were presented for $Co_6(OH)_3(TeO_3)_4(OH)$ by Perez *et al*. Moreover, in spite of their non-centrosymmetric and polar structures, no dielectric properties and magneto-dielectric coupling characterizations have been investigated for none of these Co-phases.

We present hereafter the microwave-assisted and conventional hydrothermal syntheses of $Co_6(OH)_3(TeO_3)_4(OH)\sim0.9(H_20)$. Its crystal structure was investigated from single crystal X-ray data and coupled infrared spectroscopy with thermogravimetric analyses. We also report the magnetic structure, solved from powder neutron diffraction data, the DFT calculations as well as the macroscopic magnetic and dielectric properties.

2 EXPERIMENTAL SECTION

2.1 Synthesis

To obtain a single-phase sample of $Co_6(OH)_3(TeO_3)_4(OH)\sim0.9(H_2O)$, we performed several tests by microwave-assisted hydrothermal synthesis in alkaline solution. In a first time, we studied the influence the nature of the cobalt(II) inorganic salt (i.e. $Co(NO_3)_2.6H_2O$ or $CoCl_2.6H_2O$) on the synthesis results. All syntheses were realized with the same ratio of precursors: 3 equivalents of $Co(NO_3)_2.6H_2O$ or $CoCl_2.6H_2O$ and 2 equivalents of TeO_2. We performed several syntheses by varying the amount of sodium hydroxide equivalent between 0 and 15. For this prospecting study, we used a Mars5 CEM microwave furnace. Precursors as powder samples were introduced with 30 mL distilled water in a 100 ml Teflon-lined autoclave (XP1500 by CEM). The autoclave was placed in the microwave furnace at a power of 1600W. The temperature was ramped to 185°C over 20 minutes then held for 5 hours before being cooled to room temperature following the furnace inertia. The final product was filtered and washed with distilled water and ethanol then dried in air overnight. After each synthesis, the phase identification was performed by powder X-ray diffraction. Table s1 shows the different synthesis results. A single-phase sample of $Co_6(OH)_3(TeO_3)_4(OH)\sim0.9(H_2O)$ was only obtained with the following mixing: 3 equivalents of $Co(NO_3)_2\_6H_2O$ (9.4 mmol), 2 equivalents of TeO_2 (6.26 mmol) and 7.5 equivalents of NaOH (23.5 mmol).

Single crystals were obtained from convection heating hydrothermal synthesis starting with the previous mixing, introduced with 10 ml of deionised water in a 50 mL PTFE autoclave. The insert was transferred to a Berghof pressure digestion vessel then heated from room temperature to 185°C in 5 hours and 20 minutes, left at 185°C for 72 hours and cooled to room temperature in 10 hours. The final product was filtrated, washed with water and ethanol then dried in air overnight. Finally, we obtained small purple rod-like single crystals of 10 ×

$10 \times 90\ \mu m^3$. By increasing the synthesis temperature to 230°C we obtained bigger single crystals of $20 \times 20 \times 150\ \mu m^3$ suitable for dielectric property measurements.

2.2 Single crystal X-ray diffraction

The single crystal X-ray diffraction experiments were performed on a Bruker-Nonius KappaCCD four circles diffractometer equipped with an Apex2 detector and an INCOATEC microfocus source (Mo-λK_α = 0.71073 Å). The diffraction data were collected at room temperature on a single crystal of suitable size ($5 \times 5 \times 90\ \mu m^3$). The data collection strategy was defined to get a data set corresponding to a complete reciprocal sphere up to high theta angle and with high redundancy. Details of the data collection are summarized in Table 1. Intensity diffraction data were integrated with the software SAINT[10] and were corrected from absorption using SADABS program[11] developed for scaling, corrections for twin and area detector data.

2.3 Powder neutron diffraction

The powder neutron diffraction (PND) data were recorded on the 3T2 and G41 diffractometers at the Leon Brillouin Laboratory (LLB) Saclay, France. On 3T2 the PND pattern was recorded at room temperature with a 2θ range of 5 – 122° and a wavelength of 1.225 Å. PND diagrams were recorded on G41 between RT and 1.7 K with 2θ ranging between 9 – 88.9° and a wavelength of 2.423 Å.

2.4 Structure solution and refinements

The structure was determined using SUPERFLIP[12] on a single crystal obtained by convection heating hydrothermal synthesis. The first atomic model obtained from SUPERFLIP with the chemical formula $Co_6Te_4O_{16}$ and the space group $P6_3mc$ corresponded to the one previously published without the hydrogen atoms by Perez *et al.*[3] The structure refinements were then performed using the program Jana2006[13] with anisotropic displacement parameters (U_{aniso})

used for all atoms (Table s2). The bond valence sums (BVS)[14] calculated with parameters provided by Brese and O'Keeffe[15] clearly evidenced an electron deficit on the atom O4. This deficit suggests the presence of a hydrogen atom linked to O4. The position of this hydrogen atom was found from the Fourier difference map. Another residue close to the O5 atom in the large tunnel was also found from the Fourier difference map. It corresponds to the O6 atom of the water molecule. This latter was introduced in our model and its occupancy factor was refined. Anisotropic displacement parameters were assumed for all atoms except for O6 and H-o4, and the final refinement cycle leads to the following *R* factors: R_{obs} = 1.33 % and wR_{obs} = 1.89 %. The chemical formula was $Co_6(OH)_3(TeO_3)_4(OH).0.88(H_2O)$ with an amount of water very close to the one found from the TG curve (see section 3.3). Atomic positions and atomic displacement parameters ($U_{iso,eq}$) are listed in Table 2 and U_{aniso} in Table s2. A selection of interatomic distances and bond valence sums are presented in Table 3. We can note that the O5 atom present large anisotropic displacement parameter along the *c*-axis. It shows that the OH^- groups in the large hexagonal tunnel are delocalized along the *c*-axis.

The Rietveld refinements were performed from combined PND data recorded on G41 and 3T2 diffractometers. These data were collected on a polycrystalline sample obtained by assisted microwave-assisted hydrothermal synthesis. The same structural framework was obtained as previously from single-crystal diffraction data. Nevertheless, there were some slight differences in the amount of water and the localization of the oxygen atoms of the OH^- groups and H_2O molecules in the large tunnels. This could be due to a different hydration rate between different samples. Rietveld refinement parameters, the corresponding atomic positions and atomic displacement parameters (U_{iso}) are listed in Table s3.

2.5 AGIR technique

In order to improve information relative to the water and hydroxide stoichiometry in $Co_6(OH)_3(TeO_3)_4(OH)\sim0.9(H_2O)$, AGIR measurements were carried out. The AGIR is a

technique recently developed and consists of a Setaram microbalance head adapted to an infrared (IR) reactor-cell allowing to measure simultaneously the weight and IR spectra of a solid sample under gas flow, between room temperature and 773 K. The setup has been described in detail by Bazin et al. [16] and has shown to be of interest in several works related to the quantification of adsorbed species on different materials.[17,18,19,20,21] Analyses were carried out on self-supported pellets (2 cm^2, 20-25 mg). MIR spectra of the sample were recorded IR every 60 seconds with a Nicolet 6700 spectrometer equipped with a MCT detector (64 scans/4 cm^{-1} resolution). In parallel, the outlet gas flow composition was continuously provided by a MS analyzer (Pfeiffer Omnistar GSD301). In this work, the $Co_6(OH)_3(TeO_3)_4(OH)\sim0.9(H_2O)$ sample was heated at a rate of 2 K/min from 298 to 773 K under an argon flow of 20 ml/min

2.6 Electronic structure calculation

The electronic structure of $Co_6(OH)_3(TeO_3)_4(OH)\sim0.9(H_2O)$ was calculated through the density functional theory (DFT) as implemented in CRYSTAL software[22]. Since the cobalt 3d shells are strongly correlated, we used hybrid functional (B3LYP approximation) to correct the self-interaction problem. The wave functions were expanded as a linear combination of Bloch functions using Gaussian-type atomic orbitals. We chose an all-electron and triple zeta valence with polarization for cobalt, [23] a Stuttgart core pseudo-potentials (ECP28MDF) with a valence double zeta basis for tellurium atoms[24] and a 8-411(1d)G basis set for oxygen atoms.[25] The Coulomb and exchange series were truncated with overlap thresholds of 10^{-8}, 10^{-8}, 10^{-8}, 10^{-8} and 10^{-16} and a Monkhorst-Pack 3x3x8 sampling scheme was chosen after some tests. In our DFT calculations, we omitted the O6 oxygen atoms associated with water molecules in the channels. For the $[Co_6(OH)_3(TeO_3)_4]^+$ framework we used the experimental positions (see Table 2). The unknown positions of the hydrogen atoms of the hydroxyl groups in the channels were relaxed using the default options of CRYSTAL, preserving the

symmetry of the crystal and the ferromagnetic configuration of the Co^{2+} S = 3/2 spins. The distance between the two atoms of this group was evaluated to 0.91 Å.

2.7 Magnetic measurement

Magnetic susceptibility measurements were performed with a Magnetic Property Measurement System (MPMS) Quantum Design. 60 mg of $Co_6(OH)_3(TeO_3)_4(OH)\sim0.9(H_2O)$ polycrystalline sample were mixed with grease allowing the alignment of the crystallites under a magnetic field. The alignment was performed with a Field cooling from room temperature under 5 T before the magnetic loops recording at 2 K. The magnetic susceptibility was measured on misaligned crystallites under a magnetic field of 0.01 T from 2 K to room temperature. A Physical Properties Measurement System (PPMS) Quantum Design equipped with the VSM option was also used to performed magnetic loops up to 14T.

2.8 Dielectric measurement

Dielectric measurements were performed on a small single crystal. This latter was fixed on a small glass plate with GE varnish and two gold wires (25 µm) were attached using silver epoxy (EPOTEK H2OE) at the two extrema of the crystal. Considering the needle geometry of this crystal, the classical thin plate approximation used for calculating the dielectric constant from the capacitance is not applicable here and data will be presented as a capacitance and not converted as a dielectric constant. The capacitance was measured using an LCR meter Agilent 4282 and a home-made sample holder into the PPMS.

2.9 Structure description

The structure of $Co_6(OH)_3(TeO_3)_4(OH)\sim0.9(H_2O)$ perpendicular to the *c*-axis is shown in Figure 1. The cationic framework is related to the mineral Ellenbergerite.[9] It consists of

distorted [$Co^{II}O_6$] octahedra which form infinite zig-zag chains along the *c*-axis. (Figure 2a) Each chain is composed of [$Co^{II}O_6$] octahedra which share faces to form [$Co^{II}_2O_9$] dimers with a Co-Co distance of 2.8183(5) Å. (Figure 2b) Then the dimers shared edges with each other and extend as infinite $[Co^{II}_2O_5]_\infty$ zig-zag chain along the c-axis. The [$Co^{II}O_6$] octahedra are strongly distorted with Co-O distances that range between 2.068(3) Å and 2.225(3) Å. (Table 3) Such [$Co^{II}O_6$] distorted octahedral are also observed in the related compounds $Na_{2-x}Co_6(OH)_3[HPO_4][H_{x/3}PO4]_3$,[7] $Co_7(OH)(AsO_4)(AsO_4H)$[5] and $Co_7(OH)_2(H_2O)[VO_4]_4$.[4] For all of these compounds, the longer Co-O distances correspond to the oxygen atoms of hydroxyl groups. These OH^- groups formed H-bonds along the *c*-axis with O atoms belonging to the infinite chains $[Co^{II}_2O_5]_\infty$. For $Co_6(OH)_3(TeO_3)_4(OH)\sim0.9(H_2O)$ the H-bond O4─H1···O3 of 3.103(5) Å between the two oxygen atoms (Figure 2a) is shorter than for the other related compounds. Those chains are linked to each other via corners (Figure 2c) and formed to types of tunnels: large hexagonal along the six-fold screw axis and small triangular along the three-fold axis. The Te1 atoms lay in the large hexagonal tunnels with bridging [$Te1^{IV}O_3$] polyhedra between two double chains $[Co^{II}_2O_5]_\infty$ by sharing corners (Figure 2c). The lone pairs point out through the centres of the tunnels. The other Te2 atoms lay on a 3-fold axis inside the triangular channels (Figure 2c). Each [$Te2^{IV}O_3$] polyhedra present their triangular base perpendicular to the *c*-axis with lone pairs pointing out the opposite direction of the *c*-axis. The [$Te^{IV}O_3$] polyhedra are regular. Indeed, the [$Te1^{IV}O_3$] polyhedra are formed of two Te1-O2 bonds of 1.867(4) Å and one Te1-O1 bond of 1.894(3) Å. The [$Te2^{IV}O_3$] polyhedra are formed of three Te2-O3 bonds of 1.873(3) Å.

As for the other related compounds, the framework $[Co_6(OH)_3(TeO_3)_4]^+$ is positively charged. In our case, the electro-neutrality is maintained by one OH^-. These hydroxyl groups are situated in the large hexagonal tunnels with the water molecules. As shows the large anisotropic displacement parameter along the *c*-axis, the OH^- groups localized on the centre of

the hexagonal tunnels but are highly delocalized along the tunnel-axis. The water molecules are positioned out of the centre of these tunnels, between the OH^- groups.

3 RESULTS AND DISCUSSION

3.1 AGIR

To confirm the presence of additional water molecules in $Co_6(OH)_3(TeO_3)_4(OH)\sim0.9(H_2O)$ we performed simultaneously: temperature dependent measurements of gravimetric analysis, mass spectroscopy and IR spectroscopy with the AGIR device. The IR spectra, TGA and DTG curves, the evolution of the MS signal for water and the variation of IR bands intensity during the thermal treatment are reported Figure 3 and Figure 4.

The FTIR measurements confirm the presence of water molecules in our sample. Indeed the small band observed at 1617 cm^{-1} corresponds to the bending vibrations of the water molecules $\delta(H_2O)$. This band disappears after heating over 120°C (Figure 4a). According to the mass variation (Figure 4a), the amount of water molecules adsorbed is relatively small. The DTG curve emphasizes two main mass variations at 170°C and 460°C. The desorption of water at 170°C is concomitant to the disappearance of the O-H stretching bands at 3631 cm^{-1}. The two O-H stretching bands at 3522 and 3460 cm^{-1} which are still present over 100°C should correspond to the OH groups. Assuming the correlation function given by Libowitzky[26] $\nu(cm^{-1}) = 3545 - 1.19\cdot10^{12}\cdot\exp(-d(O\cdots O)/0.1230)$ which linked the O-H stretching frequencies and the O-H···O hydrogen bond lengths it's possible to attribute these two bands to specific OH^- groups. The calculated frequency for d(O4···O3) = 3.103(5) Å is ν = 3531 cm^{-1}. Thus, the band at 3522 cm^{-1} can be attributed to the OH^- group linked to the cobalt atom. This agrees with the FTIR measurements of $Ni_6(OH)_3(SeO_3)_4(OH)$[8] where the O-H stretching band corresponding to the OH^- groups linked to the nickel appeared at 3520 cm^{-1}. Still for $Ni_6(OH)_3(SeO_3)_4(OH)$ the stretching band corresponding to the OH^- anions in the

tunnel is sharp and observed at 3540 cm^{-1}. For $Co_6(OH)_3(TeO_3)_4(OH)\sim0.9(H_2O)$ the band is broader and shifted around 3460 cm^{-1}. The lowering stretching frequency indicates a reinforcement of the hydrogen-bond strength for the OH^- groups in the tunnels of $Co_6(OH)_3(TeO_3)_4(OH)\sim0.9(H_2O)$. Moreover, the broadening of this band confirms that the OH^- positions in the tunnels of $Co_6(OH)_3(TeO_3)_4(OH)\sim0.9(H_2O)$ are more delocalized compare to $Ni_6(OH)_3(SeO_3)_4(OH)$. The overtone bands, 2ν(OH), involving the stretching vibrations of the hydroxide groups are also observed around 1360 cm^{-1}. The last bands observed on the FTIR spectrum below 1000 cm^{-1} correspond to trigonal-pyramidal [$Te^{IV}O_3^{2-}$] anions. The symmetric stretching vibrations $\nu_s(Te^{IV}O_3)$ correspond to the band around 893 cm^{-1}. The antisymmetric stretching vibrations $\nu_{as}(Te^{IV}O_3)$ generate split bands at 819 and 757 cm^{-1}.

On the TG curve, we observe a first mass loss at 100 °C (Δm ~ 0.5 %) followed by slightly mass loss until 195°C where the most important mass loss takes place (Δm ~ 3.1 %). The total mass loss is Δm = 4.2 % and corresponds to the sum formula $Co_6(OH)_3(TeO_3)_4(OH)\_0.64(H_2O)$. Simultaneous mass spectrometry measurements have confirmed that these mass losses correspond to water loss.

3.2 Magnetic behaviour

The molar magnetic susceptibility is reported in Figure 5. It shows the presence of a magnetic transition at a temperature T ≈ 70 K and of broad anomalies at T ≈ 40 K and 12 K. At high-temperature T > 150 K, a Curie-Weiss behaviour characteristic of a paramagnetic regime is observed (Inset of Figure 5). From the linear fit of $1/\chi_{mol}$ as a function of temperature, a molar Curie constant $C_{mol} \approx 9.0$ emu.mol^{-1}.K and a Weiss temperature $\theta_W \approx$ -90 K can be inferred. This corresponds respectively to an effective moment $\mu_{eff} = 4.9\ \mu_B$/Co and

to the existence of antiferromagnetic fluctuations. Considering the Co^{2+} double chains structure with predominant zigzag like AF exchange coupling, we apply the semi-empirical Emori approach[27,28] for the spin susceptibility of S = 3/2 antiferromagnetic Ising chains (Figure 6).

Magnetic susceptibility multiplied by temperature was fitted by the following expression:

$$\chi_{1D}.T = \frac{N\, g^2 \mu_B^2\, S(S+1)}{3k}\, e^{J^*/kT} = C_{mol}\, e^{J^*/kT}$$

where J* is an effective coupling related to the true intrachain exchange coupling J by $J = 3J^*/S(S+1)$ (N is the Avogadro number, g the Landé factor, μ_B the Bohr magneton and k the Boltzman constant). An interchain coupling J' can be introduced with a molecular field approach [29] leading to

$$\chi_{mol}.T = \frac{\chi_{1D}.T}{1 - \frac{2\, z'J'}{N\, g^2 \mu_B^2}\chi_{1D}}$$

We have fitted the data from 70 K to 400 K with this expression. (z' = number of nearest neighbours). The result is shown in Figure 6, and we find $C_{mol} \approx 8.63$ emu.mol^{-1}.K that corresponds to $\mu_{eff} \approx 4.8\ \mu_B$/Co. This is very close to the value obtained by the Curie-Weiss model $\mu_{eff} \approx 4.9\ \mu_B$/Co, and in good agreement with the current value for high spin Co^{2+} in octahedral environment with a significant spin-orbit coupling ($\mu_{eff} = 3.87\ \mu_B$ for Co^{2+} with a Spin only moment and 6.63 μ_B for the free ion with the full orbital contribution). At this point, it is worth noting that these effective moments in the paramagnetic state indicate an unquenched orbital contribution (indeed expected for Co^{2+} in a slightly distorted octahedral environment). The exchange couplings are found to be $J = -51 \pm 0.3$ K which corresponds to the general antiferromagnetic coupling and $z'J' = 1.8 \pm 0.4$ K to a very small effective ferromagnetic coupling which remains between the chains.

In Figure 7 is shown the magnetization loop at T = 2 K. We observe no coercive field B_c (or, at least, $B_c < 50$ G), a fully reversible loop, two relatively broad anomalies and a weak remnant magnetization $M_r \approx 0.06\ \mu_B$/Co. Its variation as a function of temperature is reported in Figure 8. We note that M_r goes through zero at T = 75.5 K, which is then by definition the critical temperature of the ordered state and in good agreement with the PND data. Another anomaly is seen at T ≈ 12 K, more clearly as the one observed under applied field (Figure 5). Thus, our compound has a very weak ferromagnetic component that could be attributed to the presence of an antiferromagnetic canted state with a change of canting angle at T ≈ 12 K. Note that $Co_6(OH)_3(TeO_3)_4(OH)\sim0.9(H_2O)$ presents structural similarities with other complex Co^{2+} compounds such as the arsenate $Co_7(OH)(AsO_4)(AsO_4H)$[5], vanadate $Co_7V_7O_6(OH)_2(H_2O)$[4] and cobalt sodium phosphate hydroxide $Na_{2-x}Co_6(OH)_3(HPO_4)(H_{x/3}PO_4)$[7]. All these materials have been described with an antiferromagnetic canted ground state at low temperature.

Note also a broad change in the temperature variation of M_r occurring around 40 K in our compound (Figure 8). To get further, let us return to the magnetization loop at T = 2 K (Figure 7) which shows two broad slopes changes at 2 fields, noted B_1 and B_2. This metamagnetic-like behaviour can be followed by measuring magnetization loops at different isotherms. The corresponding phase diagram is reported in Figure 9. We conclude that the anomalies in magnetic susceptibility and magnetization correspond to three different canted antiferromagnetic states named AF1, AF2 and AF3 in Figure 9. No saturation of the magnetization has been observed up to 14 T ($M_{(14T)} \approx 2.25\ \mu_B$/Co, not shown here). This is the largest field accessible in our laboratory, and the possibility of other magnetic field induced states cannot be excluded.

3.3 Magnetic structure

The PND diagrams at RT and 1.7 K are shown in Figure 10. All magnetic contributions are growing on nuclear Bragg peaks in agreement with a magnetic propagation vector k = (0,0,0). The magnetic structure of $Co_6(OH)_3(TeO_3)_4(OH)\sim0.9(H_2O)$ was solved from the PND data recorded on the G41 diffractometer (λ = 2.423 Å) at 1.7 K. The representation analysis was performed with the Jana2006 program.[13] Among the different Shubnikov space groups compatible with the nuclear space group $P6_3mc$ and the k-vector (0,0,0). In a first time, we tried to refine the magnetic structure with magnetic space groups which allow ferromagnetic component: Cmc'21' (Ma ≠ 0) and Cm'c'21 (Mc ≠ 0). Nevertheless, the refinements remain very unstable. Only refinements with the $P6_3'mc'$ space group, which do not allow ferromagnetic component, gave a coherent magnetic structure corresponding to a fully compensated antiferromagnetic ordering. With this model, that corresponds to the average magnetic structure, there is only one magnetic cation position with three independent values for M_x, M_y and M_z. The result of the magnetic structure refinements is shown in Figure s2. At 1.7 K the principal component of the total magnetic moment is M_z = 2.90(2) μ_B. The two other components are smaller but significant enough to improve the refinement: M_x = 0.5(1) μ_B and M_y = 0.78(7) μ_B. The total magnetic moment obtained after refinements for the Co^{2+} cation is 2.98(14) μ_B and is consistent with the spin only magnetic moment of 3 μ_B in high spin configuration. At this point, it is worth noting that this magnetic moment indicates a quenched orbital contribution. However, the effective moment in the paramagnetic state (μ_{eff} ≈ 4.8 μ_B/Co) calculated from the magnetic susceptibility measurements is consistent with an unquenched orbital contribution (indeed expected for Co^{2+} in a slightly distorted octahedral environment). Similar behaviour has been already reported for high spin Co^{2+} materials[30]. This has been assigned either to site disordering leading to the imperfect summation of ordered magnetic moments[31] or to superexchange interactions that quench the orbital contribution[32]. Refinements of the magnetic structure were also carried out at temperatures

between 1.7 and 70 K. The global magnetic moments as well as the correspondent M_x, M_y and M_z components are plotted on Figure s3 as a function of the temperature. The fit of the curve corresponding to the total magnetic moment allowed us to determine the Néel temperature T_N = 72 K of the ordered magnetic state, in agreement with the previous magnetization measurements. Figure 11 shows the average magnetic structure of $Co_6(OH)_3(TeO_3)_4(OH)\sim0.9(H_2O)$. As we can see all magnetic moments are roughly aligned along the *c*-axis with a canting angle of 11.4°. In the infinite $[Co^{II}_2O_5]_\infty$ zig-zag chain, (Figure 11b) along the *c*-axis, two nearest-neighbour moments align parallel on the J_2 bond and antiparallel on the J_4 bond. Inside the $[Co_2O_9]$ dimers in the (*ab*) plane, the moments are coupled antiparallel via an antisymmetric Dzyaloshinsky-Moriya interaction (J_1 bond). In the continuation of the (*ab*) plane, the moments of two neighbouring chains are aligned antiparallel (J_3 bond). Into each infinite $[Co^{II}_2O_5]_\infty$ zig-zag chain, the canting give rise to a net magnetic moment in the (*ab*) plane symbolized by the orange arrow on Figure 11b. Nevertheless, as we can see in Figure 11a, around the three-fold axis of the tunnels, the sum of these magnetic moments of three double chains in the (*ab*) plane is null. Thus, over the entire magnetic unit cell, we have a fully compensated antiferromagnetic structure. As we already mentioned, this model corresponds to the average magnetic structure since the previous magnetization measurements show weak ferromagnetic component for $Co_6(OH)_3(TeO_3)_4(OH)\sim0.9(H_2O)$ with non-zero remnant magnetization ($M_r \leq 0.06\ \mu_B$/Co) below T_N. (Figure 8) Similarly, no transition is evidence from the PND diagrams between 15 and 1.7 K. It seems that the accuracy of the PND data do not allow us to detect such small variation of remnant magnetization. This could be due to the background high level. To reduce it we try to deuterate our sample, but the exchange rate D/H was too small to reduce the diffuse scattering of the H atoms. Thus, it's possible that some extra magnetic peaks are drowned into the background. We effectively see some variations in the background at low

temperatures. Nevertheless, they remain too small to be definitely attributed to magnetic peaks.

To complete this experimental model of the magnetic structure we also performed B3LYP calculations to evaluate precisely the total energies of the ferromagnetic (F) and of different antiferromagnetic (BS_i on the Figure s4) spin states with an energetical threshold fixed to 10^{-10} u.a.. The calculations lead to $E(F) - E(BS_1) = 156.1867$ meV, $E(F) - E(BS_2) = -65.1859$ meV, $E(F) - E(BS_3) = 44.3907$ meV and $E(F) - E(BS_4) = 99.1947$ meV. The BS_1 state is found to be the periodic B3LYP ground state of $Co_6(OH)_3(TeO_3)_4(OH)$~$0.9(H_2O)$ and agrees with the magnetic structure solved from PND data, i.e. J_1, J_3 and $J_4 < 0$ and $J_2 > 0$. The average calculated magnetic moment of 2.75 μ_B is derived from Mulliken analysis and is close to the experimental value of 3.01(14) μ_B extracted from the PND data.

The properties of magnetic systems are usually described by spin models. In this work, we used the Ising Spin Hamiltonian written as a sum of $-J_{ij}\,\hat{S}_{z,i}\hat{S}_{z,j}$ terms with the B3LYP calculations to determine the different magnetic exchange constants J_{ij} between the Co^{2+} cations. A negative magnetic exchange constant J_{ij} means therefore an antiferromagnetic coupling. As the exchange constants are expected to decrease with the distance between the two magnetic sites, only four magnetic pathways were taken into account (Figure 11) in $Co_6(OH)_3(TeO_3)_4(OH)$~$0.9(H_2O)$: the exchange constant J_1 between the two Co sites of the inside the $[Co^{II}{}_2O_9]$ dimer (Figure 11b); J_2 and J_4 between two Co sites of two successive $[Co^{II}O_6]$ octahedra respectively along the chain axe (*c*-axis) and along the diagonal; J_3 between two Co sites of two different chains. (Figure 11a)

To extract the exchange constants J_{ij}, we related energy differences between the ferromagnetic state and the various broken symmetry configurations (BS_i) and the exchange constants via a mapping procedure described by P. R. Moreira et al.[33] :

$$E(F) - E(BS_1) = -2\,S^2(6\,J_1 + 6\,J_3 + 12\,J_4)$$

$$E(F) - E(BS_2) = -2\,S^2(6\,J_1 + 6\,J_3 + 12\,J_2)$$

$$E(F) - E(BS_3) = -2\;S^2(12\,J_2 + 12\,J_4)$$

$$E(F) - E(BS_4) = -2\;S^2(\,4J_1 + 4\,J_2 + 12\,J_4)$$

in which S^2 is the square of the spin for each magnetic site. Finally, we were able to propose the following values for the exchange constants: J_1 = 2.7 K, J_2 = 19.0 K, J_4 = -28.6 K, J_3 = -12.7 K. Within the infinite $[Co^{II}_2O_5]_\infty$ zig-zag chains, the main coupling is antiferromagnetic and is assigned to the one (J_4) along the diagonal of the chain. Along the *c*-axis, the coupling inside the chain corresponding to J_2 is ferromagnetic. Weaker ferromagnetic interactions are also found in these chains with J_1 = 2.7 K. We can notice that the interaction between the two Co sites of the inside the $[Co^{II}_2O_9]$ dimer (J_1) is weakly destabilizing in BS_1 spin state. In the magnetic structure, this interaction (J_1 bond) stay frustrated and the antisymmetric Dzyaloshinsky-Moriya exchange allow to stabilize the interaction. Between these chains, the coupling (J_3) also remains antiferromagnetic.

Finally, the spin canting is often found in Co^{II}-based magnetic structures.[4,34] It's caused by Co^{II} magnetic anisotropy and/or antisymmetric exchange in the magnetic sublattice. Since this structure is non-centrosymmetric, the canted antiferromagnetic behaviour could be related to the Dzyaloshinsky-Moriya interaction. Such interaction has been evidenced in the average magnetic structure. We can assume that the real magnetic structure remains highly anisotropic with the c-axis as easy magnetization axis and that the magnetic moments are not completely compensated in the (*ab*) plane.

3.4 Dielectric measurements

Because of the very small size of the crystals (typically 20 × 20 × 100 µm^3), the magnetic measurements have been performed on powder samples. Nevertheless, we succeed in attaching two gold wires on one sample to perform dielectric measurements in this highly

insulating sample. From the complex impedance, we find that our sample is essentially capacitive at low temperature with dielectric loss tangent tan $\delta < 0.05$. In Figure 12 is shown the variation of the deduced dielectric capacitance C_p as a function of temperature. C_p is modified at the three temperatures (75, 40 and 12 K) corresponding to the above-mentioned magnetic transitions, with small but sizeable relative changes of the dielectric constant $\Delta\varepsilon/\varepsilon < 1$ %. This evidences a magneto-structural coupling as often observed in antiferromagnets with non-collinear spins order and confirms that dielectric spectroscopy is extremely efficient in detecting tiny structural changes. We have also measured the magnetic field variation of capacitance up to 14 T in the different magnetic states. Within experimental resolution, we do not observe any magnetocapacitance for our measurement geometry (B perpendicular to the length of the needle crystal). If magnetocapacitance is present in our sample, it should be lower than an upper limit of $\Delta\varepsilon(14T)/\varepsilon < 0.001\%$.

4 CONCLUSION

$Co_6(OH)_3(TeO_3)_4(OH)\sim0.9(H_20)$ ($\varepsilon\sim0.9$) was obtained by different hydrothermal synthesis modes. First of all, microwave assisted heating mode allowed us to get a single-phase powder sample. In a second time, convection heating mode allowed us to grow crystals of sufficient sizes to perform single crystal X-ray diffraction experiments and dielectric measurements. This study shows the complementarity of these two techniques of hydrothermal synthesis. The structure of $Co_6(OH)_3(TeO_3)_4(OH)\sim0.9(H_20)$ is related to the Ellenbergerite structure. The magnetic measurements revealed a spin canted antiferromagnetism below $T_N = 75.5K$ as observed for all other related cobalt Ellenbergerite-like arsenate $Co_7(OH)(AsO_4)(AsO_4H)$, vanadate $Co_7V_7O_6(OH)_2(H_2O)$ and phosphate $Na_{2-x}Co_6(OH)_3(HPO_4)(H_{x/3}PO_4)$. We confirmed this magnetic order with powder neutron diffraction (PND) data. Indeed, in the average magnetic structure, we showed for the first time in this series of Ellenbergerite-like materials, the presence of antisymmetric Dzyaloshinsky-Moriya interactions in the (*ab*) plane

that could be responsible for the spin canted antiferromagnetic as the ground state. The DFT calculations with an Ising model show the presence of a frustrated spin state for the J_1 bond between the two Co^{2+} cations involved in the antisymmetric Dzyaloshinsky-Moriya interaction. Also, under applied magnetic field, Metamagnetic-like behaviour is observed for $Co_6(OH)_3(TeO_3)_4(OH)\sim0.9(H_20)$ and three canted antiferromagnetic states can be distinguished. Such metamagnetic behavior is also reported for $Co_7V_7O_6(OH)_2(H_2O)$. In spite of their non-centrosymmetric and polar structures, neither dielectric properties nor magneto-dielectric coupling characterizations had been investigated for none of these Co-Ellenbergerite phases. In $Co_6(OH)_3(TeO_3)_4(OH)\sim0.9(H_20)$ dielectric measurements evidence a magneto-structural coupling but no measurable magnetocapacitance below T_N. Nevertheless, some investigations in the Co^{II}- and Ni^{II}-related Ellenbergerite-like phases have to be performed to see if one of them present magnetoelectric coupling.

5 ACKNOWLEDGEMENTS

The authors thank Florence Porcher and Gilles André from LLB Saclay for the powder neutron diffraction measurements. The authors also thank Sylvie Colin for her contribution to the hydrothermal syntheses. The DFT calculation work was done with the support of the French national computer centre IDRIS under project n°081842 and the regional computer centre CRIANN under project n°2007013.

6 SUPPORTING INFORMATION

CCDC 1556805 contains the supplementary crystallographic data for this paper. These data can be obtained free of charge via www.ccdc.cam.ac.uk/data_request/cif, or by emailing data_request@ccdc.cam.ac.uk, or by contacting The Cambridge Crystallographic Data Centre, 12 Union Road, Cambridge CB2 1EZ, UK; fax: +44 1223 336033.

7 AUTHOR INFORMATION

Corresponding author email: nicolas.barrier@ensicaen.fr (Nicolas Barrier)

Tables

Table 1. Single crystal XRD experimental details

Formula	$Co_6(OH)_3(TeO_3)_4(OH)\sim0.9H_2O$	
Molecular weight ($g.mol^{-1}$)	1136.81	
Crystal system	Hexagonal	
Space group	$P6_3mc$ (No.186)	
Cell parameters		
a, *c* (Å)	13.164(1)	5.0321(6)
V ($Å^3$)	755.19(12)	
Z	2	
Calc. density ($g.cm^{-3}$)	4.9993	
Data collection		
Temperature (K)	293	
Diffractometer	Kappa CCD (Bruker-Nonius)	
Radiation	MoKα (0.71073 Å)	
Crystal colour	Purple	
Crystal description	Needle	
Crystal size (μm^3)	5 × 5 × 90	
Linear absorption coeff. (cm^{-1})	14.102	
Scan mode	ω φ	
Recording range θ (°)	$3.09° < \theta < 69.94°$	
h k l range	$-18 \leq h \leq 15$; $-18 \leq k \leq 18$; $-5 \leq l \leq 7$	
N° of measured reflections	5198	
Data reduction		
N° of independent reflections	717	
R_{int} (%)	3.03	
Absorption correction	Numerical method (SADABS)	
Transmission coeff. (min / max)	0.4666 / 0.7461	
Independent reflections with $I>3.0\ \sigma(I)$	709	
Refinement		
R (%) (all / obs)	1.28 / 1.30	
R_W (%) (all / obs)	1.74 / 1.75	
GOF (all / obs)	1.32 / 1.32	
Flack parameter	0.09(4)	
No° of refined parameters	55	
Difference Fourier residues ($e^-.Å^{-3}$)	−0.61; +0.64	

Table 2. Atomic positions and U_{iso}-*eq* parameters from single-crystal X-ray diffraction data refinements

Atoms	Wyckoff	Occ	*x*	*y*	*z*	$U_{iso,eq}$ (Å^2)
Co1	12*d*	1	0.56925(3)	0.64487(3)	0.05364(12)	0.00971(14)
Te1	6*c*	1	0.855179(11)	0.144821(11)	0	0.00885(9)
Te2	2*b*	1	1/3	2/3	0.09040(11)	0.00815(10)
O1	6*c*	1	0.79163(14)	0.20837(14)	0.7608(6)	0.0137(9)
O2	12*d*	1	0.6657(2)	0.94120(18)	0.7193(5)	0.0134(8)
O3	6*c*	1	0.59584(12)	0.40416(12)	0.4050(7)	0.0114(9)
O4	6*c*	1	0.52617(12)	0.47383(12)	0.8752(6)	0.0100(9)
H-o4	6*c*	1	0.8859	0.443	0.0004	0.020(13)
O5	2*a*	1	0	0	0.717(19)	0.27(2)
O6	6*c*	0.29(2)	0.8805(16)	0.9402(8)	0.003(5)	0.060(8)

Table 3. Selected interatomic distances, H-bond parameters and individual Bond Valence Sums from single-crystal X-ray diffraction data refinements

Atom1	Atom2	Distances	Atom1	Atom2	Distances
Co1	O1	2.121(3)	**Co1**	Co1	2.8186(8)
	O2	2.094(4)			
	O2	2.052(2)	**Te1**	O1	1.884(3)
	O3	2.073(2)		O2	1.874(3) ×2
	O4	2.218(2)			
	O4	2.162(2)	**Te2**	O3	1.865(2) ×3

Donor	H	Acceptor	D-H (Å)	H···A (Å)	D···A (Å)	A-H···D (°)
O4	H4	O3	0.944(3)	2.220(3)	3.103(4)	155.31(17)

Atoms	[a]BVS (u.v)	Atoms	[a]BVS (u.v)
Co1	1.908(6)	O1	1.999(10
Te1	4.124(17)	O2	2.119(11
Te2	4.261(15)	O3	2.115(9)
H-o4	1.042(6)	O4	2.000(6)

[a]Bond valence parameters: Co−O: R_0 = 1.698 Å, B = 0.37 Å; Te−O: R_0 = 1.977 Å, B = 0.37 Å; H−O: R_0 = 0.918 Å; B = 0.427 Å;. Bond Valence = $\exp((R_0 - R)/B)$; R_{max} = 2.8 Å.

Table 4. Assignment of the bands in the FTIR spectrum

Assignment	**Wavenumber (cm^{-1})**
ν(-OH) H_2O	3631 (s); 3330 (sh, w);
δ(-OH) H_2O	1617 (w)
ν(-OH) OH^- (Co-OH)	3522 (sh, m)
ν(-OH) OH^- (tunnel)	3463 (br, s)
2ν(-OH) OH^{--}	1359 (s); 1329 (sh, s)
$\nu_s(TeO_3)$	893 (s)
$\nu_{as}(TeO_3)$	819 (s); 757 (s)
ν: stretching; δ: deformation; s: symmetric; as: asymmetric.	vs: very strong; s: strong; m: medium; w: weak; br: broad; sh: shoulder.

FIGURES CAPTION

Figure 1. Structure of $Co_6(OH)_3(TeO_3)_4(OH)\sim0.9(H_2O)$ plotted with a 70% probability ellipsoid model refined from single-crystal X-ray diffraction data.

Figure 2. (a, b) Double infinite chain of $[Co^{II}O_6]$ octahedra running along the *c*-axis and (c) association of two double infinite chains $[Co^{II}{}_2O_5]_\infty$ via corners.

Figure 3. $Co_6(OH)_3(TeO_3)_4(OH)\sim0.9(H_2O)$ thermal treatment with the AGIR device under a flow of Ar (20 cm^3/min), from 25°C to 500°C at 2°C/min. Evolution of the IR spectra versus temperature.

Figure 4. $Co_6(OH)_3(TeO_3)_4(OH)\sim0.9(H_2O)$ thermal treatment with the AGIR device under a flow of Ar (20 cm^3/min), from 25°C to 500°C at 2°C/min. a) TGA and DTG curves. b) Evolution of the MS signal for water (m/z=18). c) Evolution of IR bands intensity versus temperature for A) 1617 cm^{-1}, B) 3631 cm^{-1}, C) 893 cm^{-1}, D) 3463 cm^{-1}, E) 1352 cm^{-1} and F) 1212 cm^{-1}.

Figure 5. Molar susceptibility of $Co_6(OH)_3(TeO_3)_4(OH)\sim0.9(H_2O)$ as a function of temperature (B = 0.01T). In the inset is shown the inverse of susceptibility and the dotted line is the Curie-Weiss fit.

Figure 6. Molar susceptibility times temperature as a function of temperature. The solid line is a fit using the Emori approach (see text for details).

Figure 7. Magnetization loop measured at T = 2 K after a field cooling with 5 T. In the inset is shown a zoom showing the remnant magnetization.

Figure 8. Thermal variation of the remnant magnetization M_r. In the inset is shown the derivative dM_r/dT. A critical temperature of 75.5 K is seen ($M_r = 0$). Another clear anomaly is seen at $T \approx 12$ K. The star marks a broad feature around 40 K.

Figure 9. Magnetic phase diagram of $Co_6(OH)_3(TeO_3)_4(OH)\sim0.9(H_2O)$.

Figure 10. Powder neutron diffraction (PND) patterns of $Co_6(OH)_3(TeO_3)_4(OH)\sim0.9(H_2O)$ at 289 and 1.7 K.

Figure 11. a) Average magnetic structure of $Co_6(OH)_3(TeO_3)_4(OH)\sim0.9(H_2O)$ in the (*ab*) plane, b) intra-chain antiferromagnetic interactions. Orange arrows indicate the resultant magnetic moments inside the chains and black arrows indicate the different magnetic exchange constants calculated by DFT method.

Figure 12. Capacitance as function of temperature (f = 500 kHz, tan δ < 0.05). The stars mark the temperature where magnetic transitions have been inferred from the magnetic susceptibility.

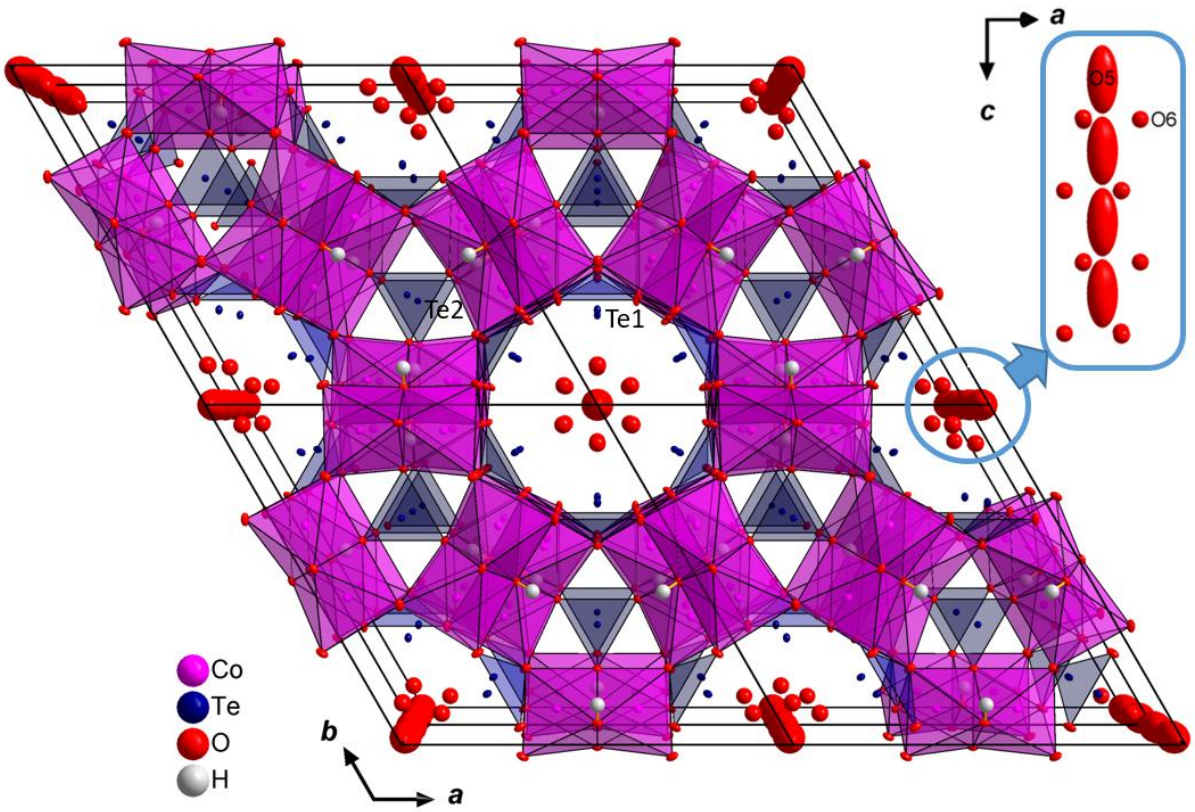

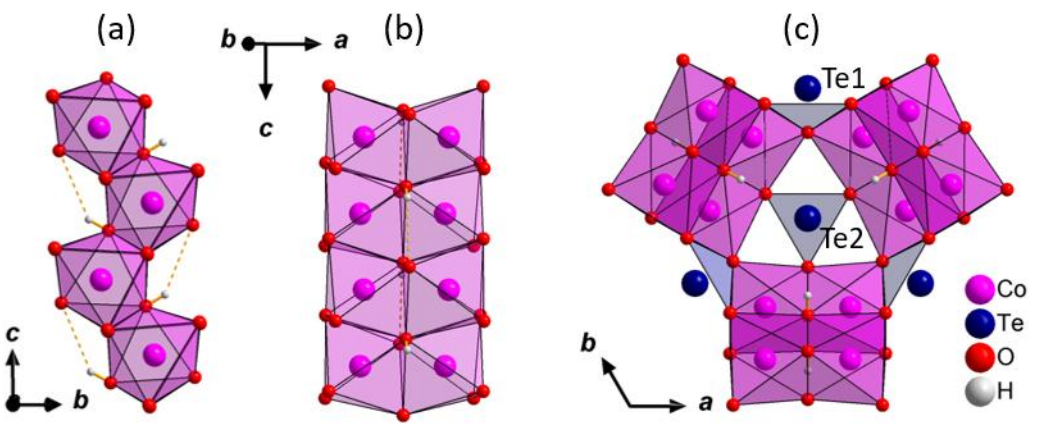

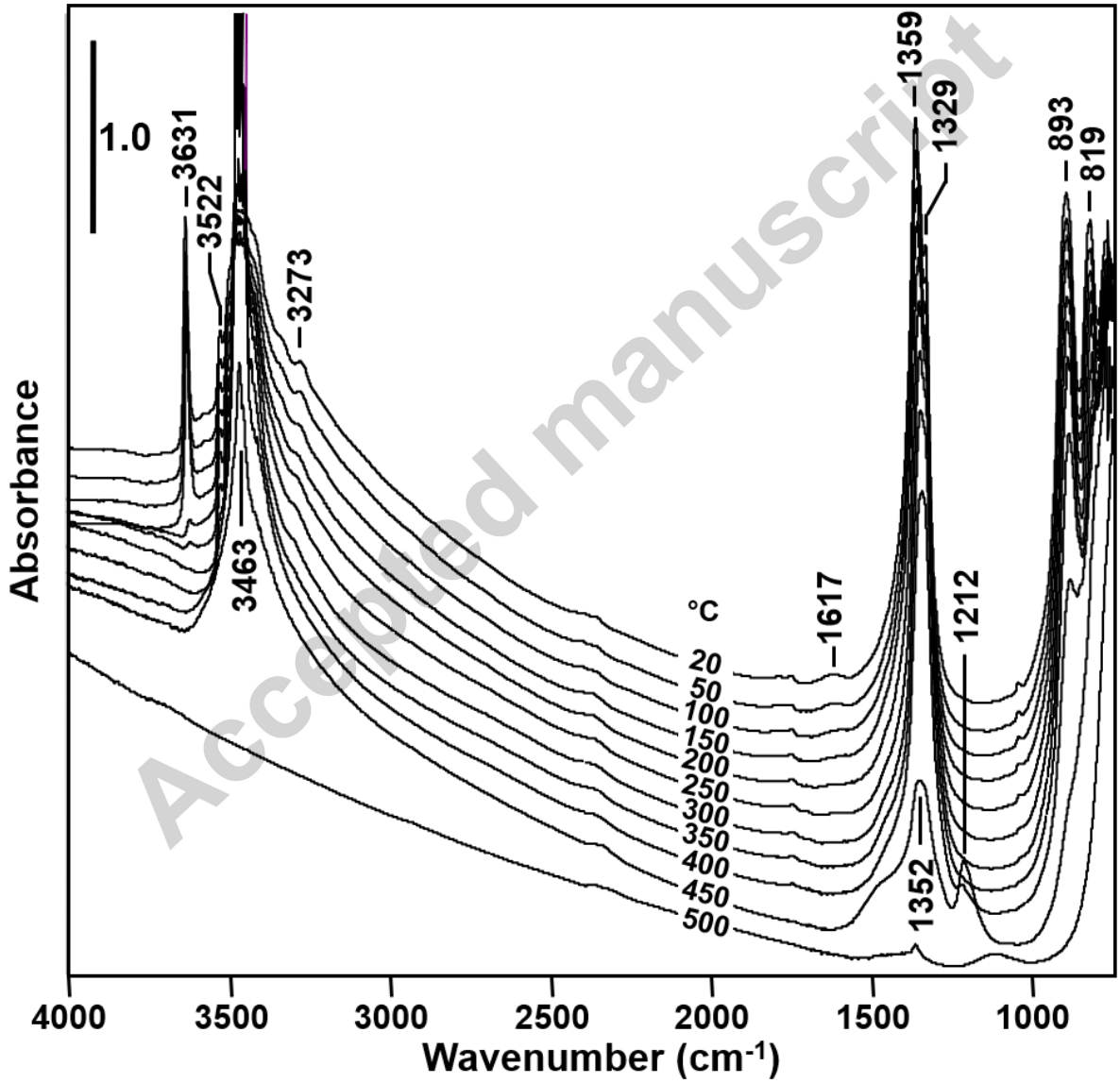

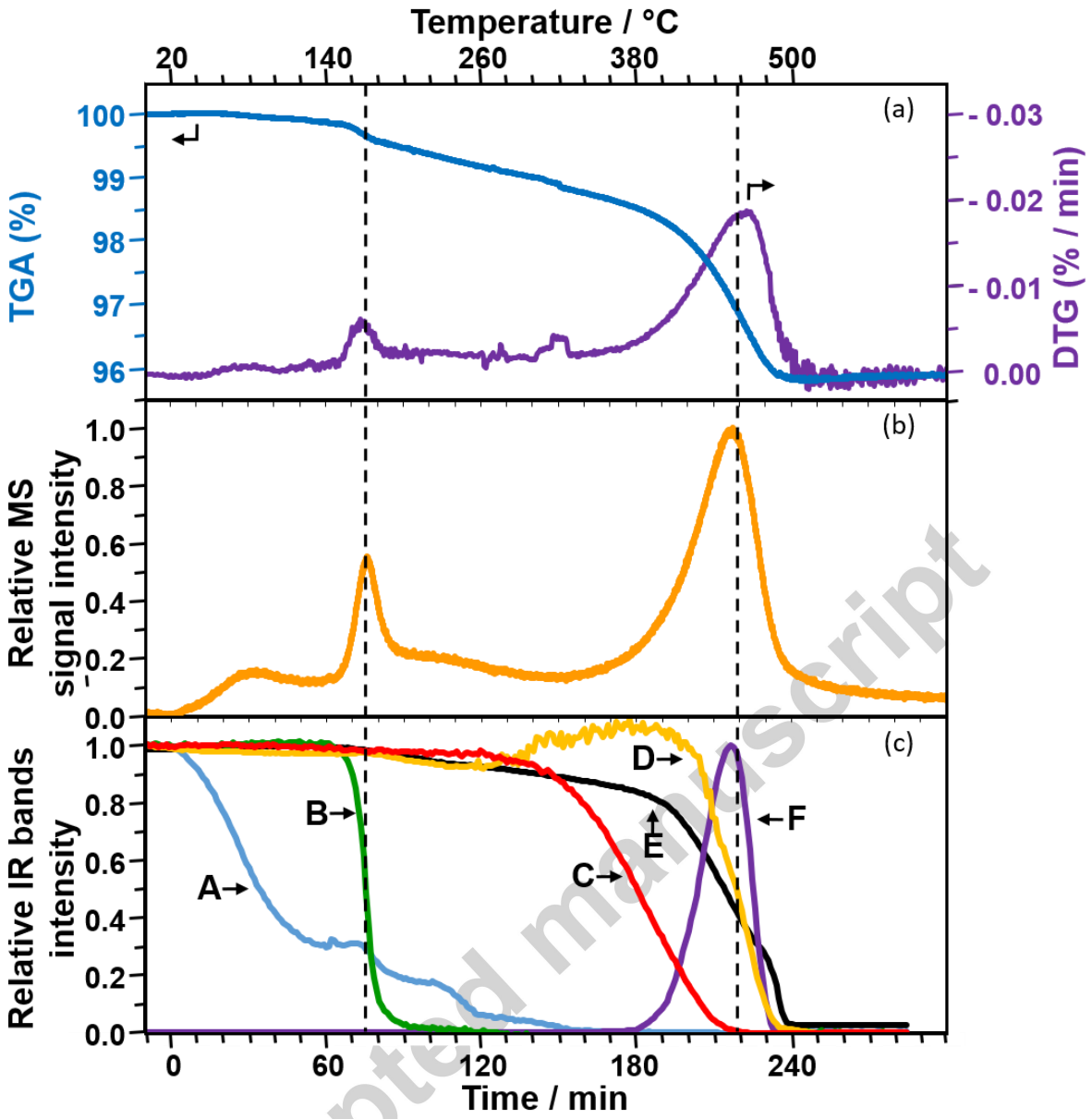

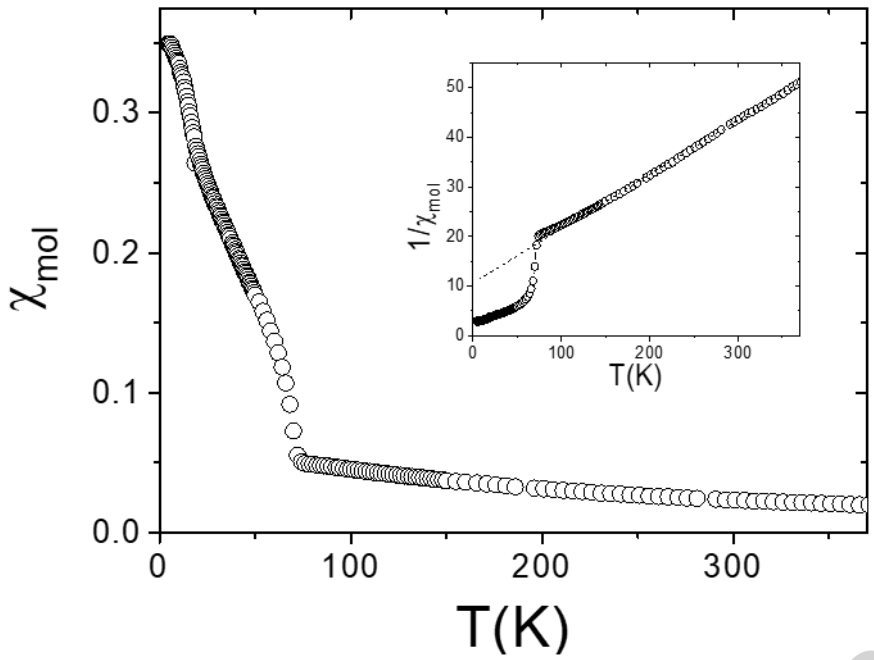

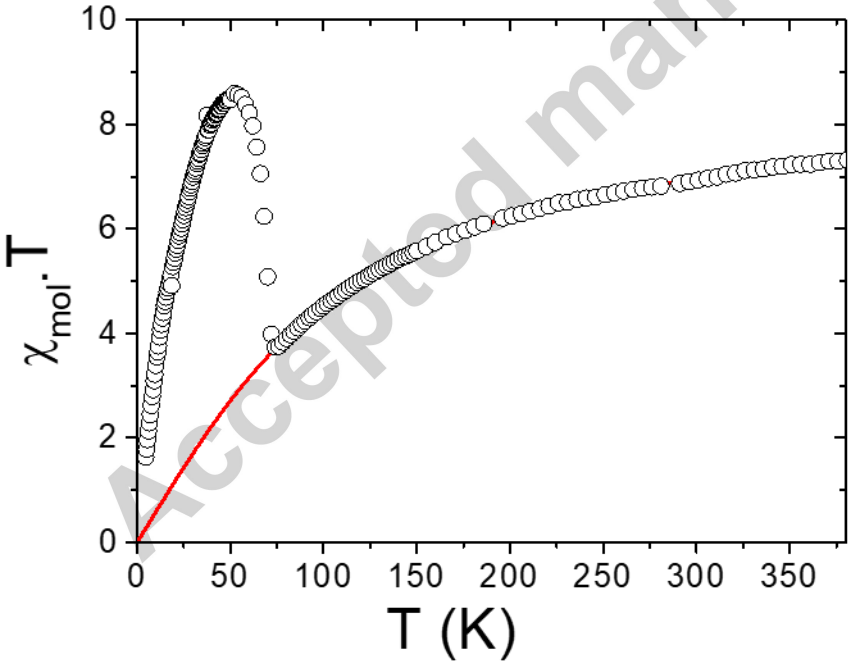

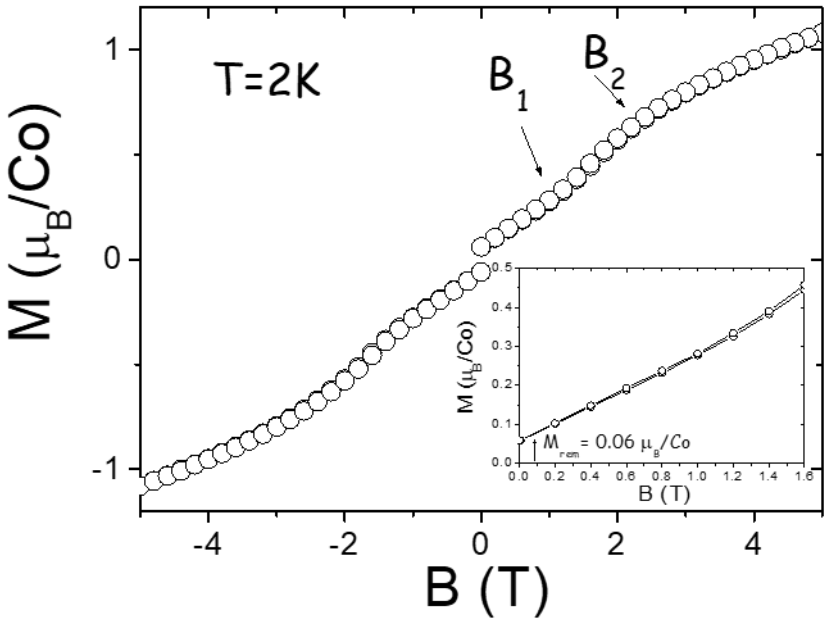

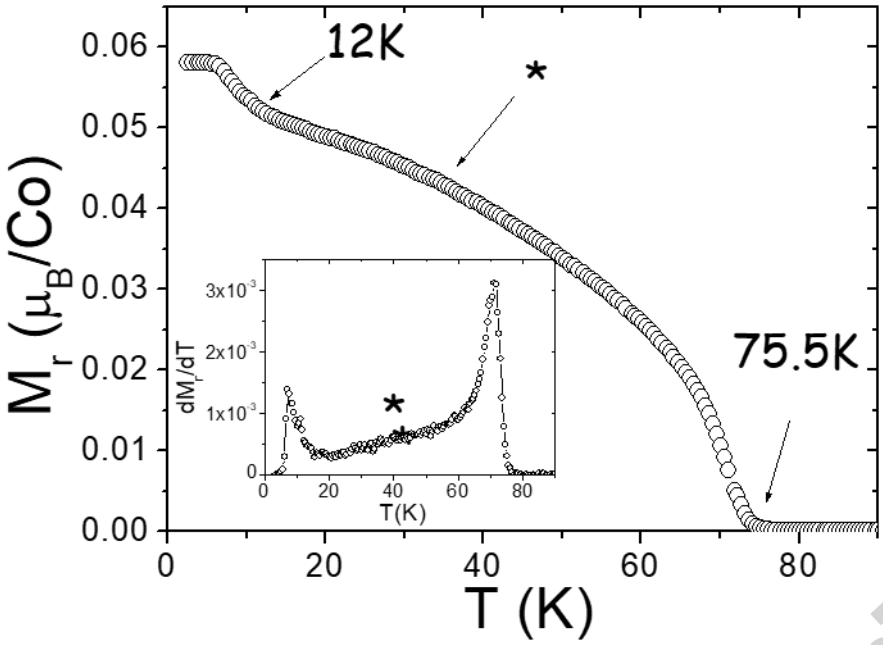

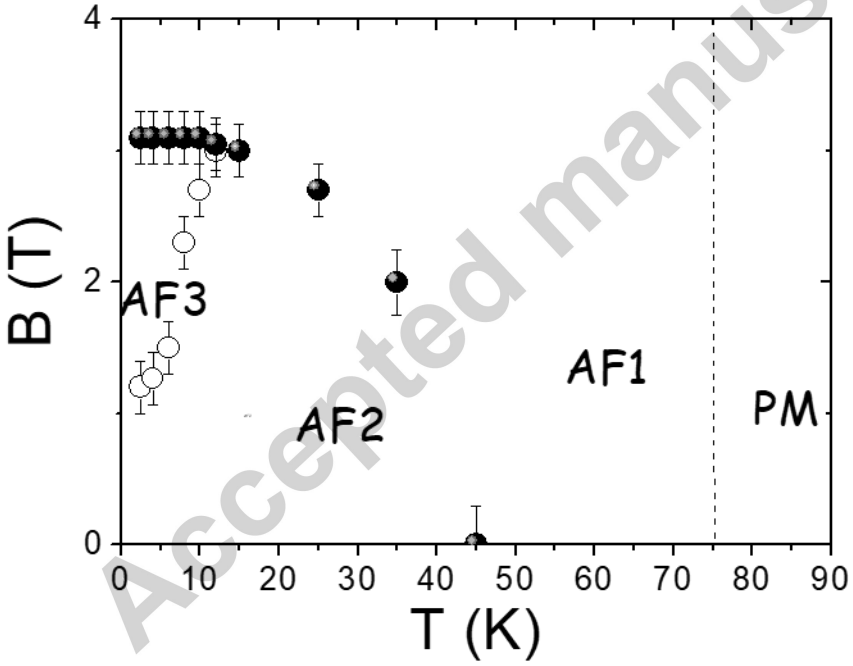

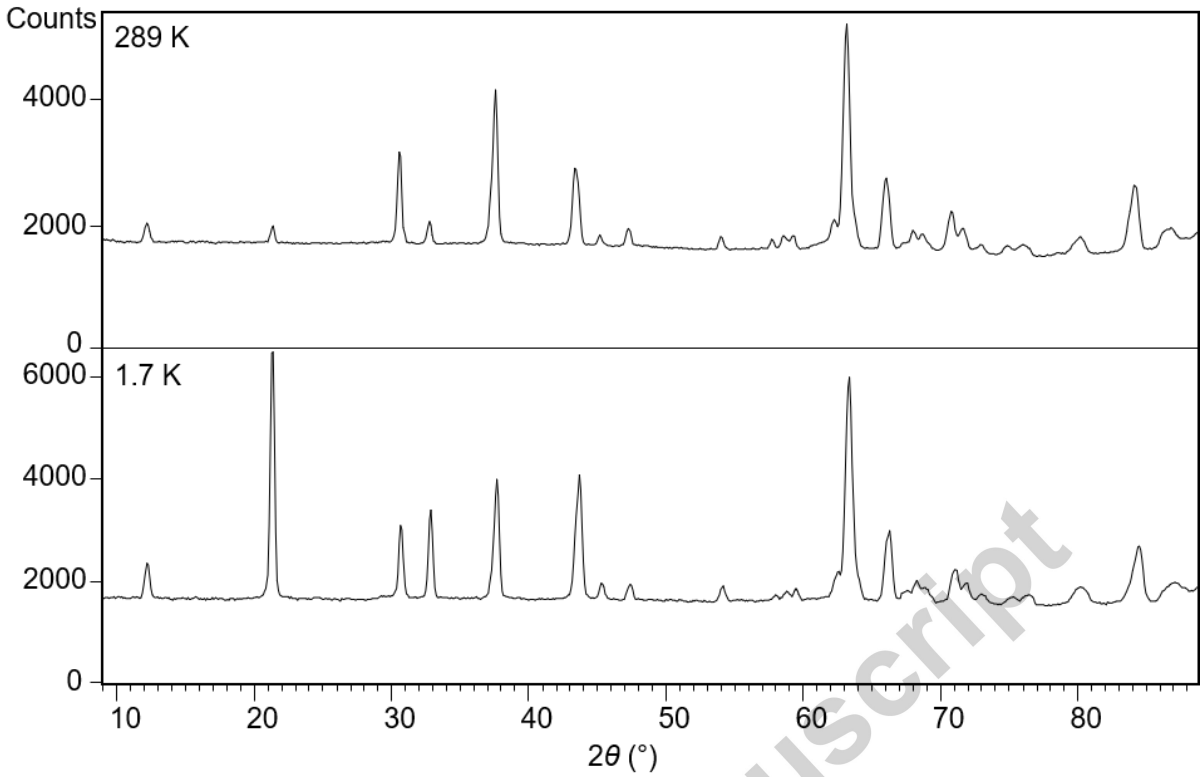
Counts
289 K
4000
2000
0
1.7 K
6000
4000
2000
0
10
20
30
40
50
60
70
80
2θ (°)

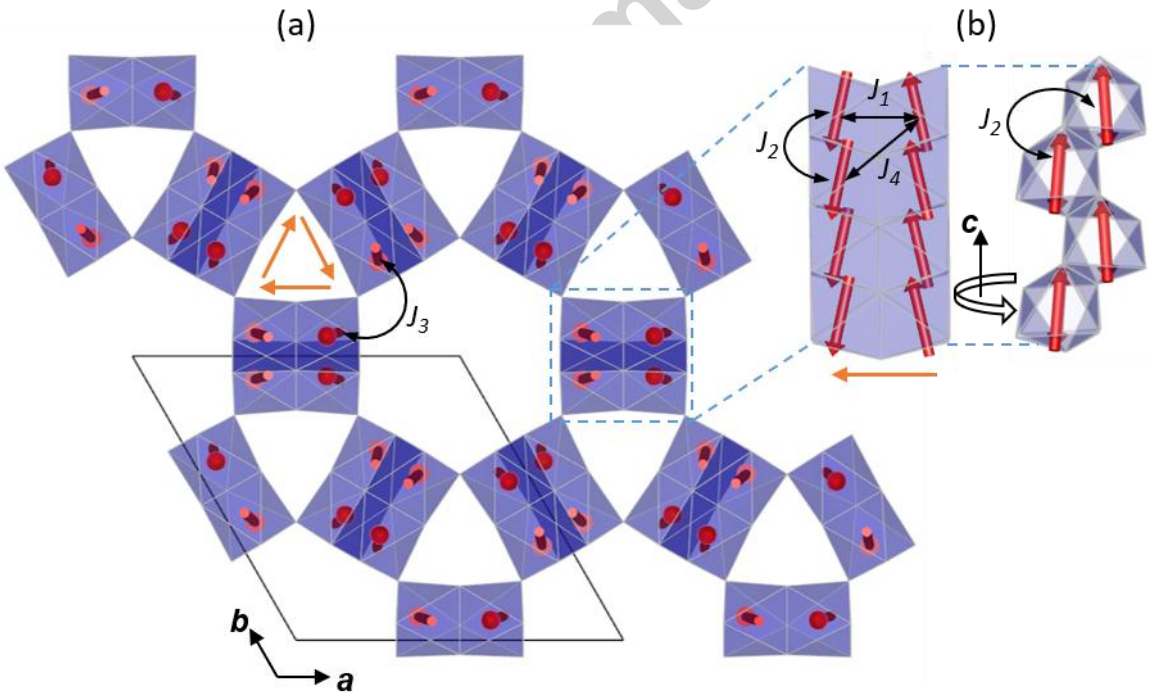
(a)
(b)
J1
J2
J4
J3
J2
c
b
a

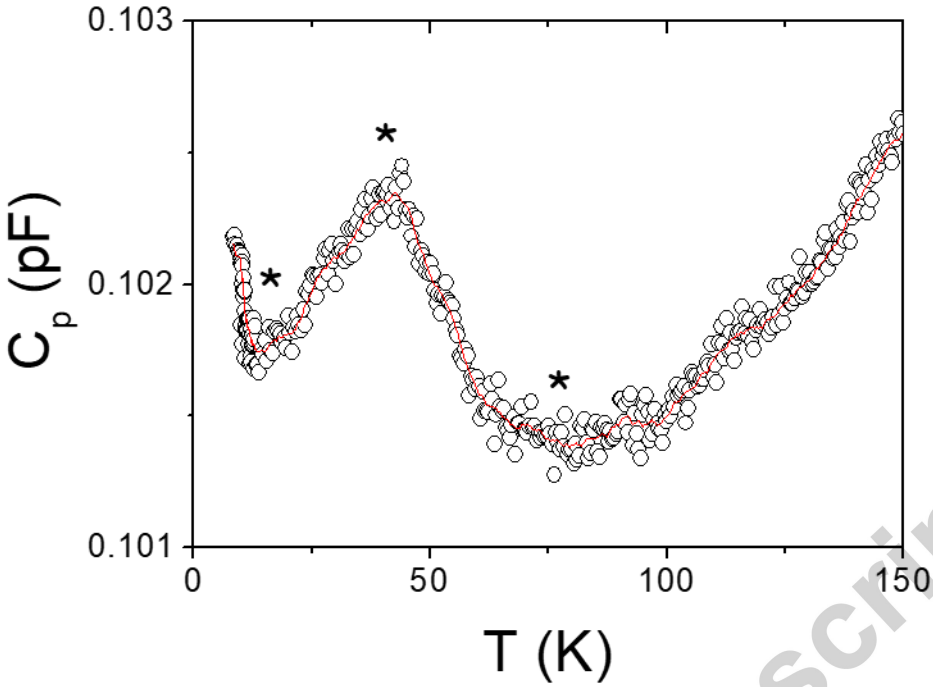

REFERENCES

(1) Hahn, T.; *International Tables for Crystallography*, *Reidel, D. Publishing Compagny: Dordecht*. **1983**.

(2) Halasyamani, P. S.; Poeppelmeier, K. R. Noncentrosymmetric Oxides. *Chem. Mater.*, **1998**, *10*, 2753-2769.

(3) Perez, G.; Lasserre, F.; Moret, J.; Maurin, M. Structure cristalline des hydroxytellurites de nickel et de cobalt. *J. Solid State Chem.* **1976**, *17*, 143–149.

(4) Zhang, S.-Y.; Guo, W.-B.; Yang, M.; Tang, Y.-Y.; Wang, N.-N.; Huang, R.-R.; Cui, M.-Y.; He, Z.-Z. Synthesis, crystal structure and magnetic property of a new cobalt(II) vanadate. *J. Solid State Chem.* **2015**, *225*, 78–82.

(5) Hughes, R. W.; Gerrard, L. A.; Price, D. J.; Weller, M. T. A Hybrid Metalloarsenate 3D Framework−1D Interrupted Metal Oxide. *Inorg. Chem.* **2003**, *42* (17), 5448–5448.

(6a) Marcos, M.D.; Amorós, P.; Beltrán-Porter, A.; MartínezMáñez R.; Attfield, J. P. Novel crystalline microporous transition-metal phosphites $M_{11}(HPO_3)_8(OH)_6$ (M = Zn, Co,

Ni). X-ray powder diffraction structure determination of the cobalt and nickel derivatives. *Chem. Mater.* **1993**, *5*, 121.

(6b) Che, R. C.; Peng L. M.; Zhou, W. Z. Synthesis and characterization of crystalline microporous cobalt phosphite nanowires. *Appl. Phys. Lett.* **2005**, 87, 173122.

(6c) Ni, Y.; Liao, K.; Hong J.; Wei, X. Ni^{2+} ions assisted hydrothermal synthesis of flowerlike $Co_{11}(HPO_3)_8(OH)_6$ superstructures and shape control. *CrystEngComm*. **2009**, *11*, 570.

(7) Yakubovich, O.V.; Kiriukhina, G.V.; Dimitrova, O.V.; Shvanskaya, L.V.; Volkova, O.S.; Vasiliev, A. N. A novel cobalt sodium phosphate hydroxide with the ellenbergerite topology: crystal structure and physical properties. *Dalton Trans.* **2015**, 44, 11827–11834

(8) Amorós, P.; Marcos, D; Roca, M.; Beltrán-Porter, A.; Beltrán-Porter, D. Synthetic Pathways for New Tubular Transition Metal Hydroxo- and Fluoro-Selenites: Crystal Structures of $M_{12}(X)_2(SeO_3)_8(OH)_6$ ($M = Co^{2+}$, Ni^{2+}; $X = OH^-$). *J. Solid State Chem.* **1996**, 126, 169-176.

(9) Chopin, C.; Klaska, R.; Medenbach O.; Dron, D. Ellenbergerite, a new high-pressure Mg-Al-(Ti,Zr)-silicate with a novel structure based on face-sharing octahedra. *Contrib. Mineral. Petrol.* **1986**, 92, 316

(10) *Brucker AXS Inc. APEX2, SAINT and SADABS; Bruker: Madison, Winsconsin, USA*. **2013**

(11) Sheldrick, G. M.; *SADABS. University of Göttingen, Germany*. **1996**

(12) Palatinus, L.; Chapuis, G. SUPERFLIP - a computer program for the solution of crystal structures by charge flipping in arbitrary dimensions. *J. Appl. Cryst.* **2007**, *40*, 786-790.

(13) Petříček, V.; Dušek, M.; Palatinus, L. Crystallographic Computing System JANA2006: General features. *Z. Kristallogr.* **2014**, *229* (5), 345–352.

(14) Brown I. D. VALENCE: a program for calculating bond valences. *J. Appl. Crystallogr.* **1996**, 29, 479-480.

(15) Brese, N. E.; O'Keeffe, M. Bond-valence parameters for solids. *Acta Cryst.* **1991**, *B47*, 192-197.

(16) Bazin, P.; Alenda, A.; Thibault-Starzyk, F. Interaction of water and ammonium in NaHY zeolite as detected by combined IR and gravimetric analysis (AGIR). *Dalton Trans*. **2010**, *39*, 8432−8436.

(17) Popov, A.; Kondratieva, E.; Goupil, J. M.; Mariey, L.; Bazin, P.;Gilson, J. P.; Travert, A.; Mauge, F. Bio-oils Hydrodeoxygenation: Adsorption of Phenolic Molecules on Oxidic Catalyst Supports. *J. Phys.Chem. C.* **2010**, *114*, 15661−15670.

(18) Moulin, B.; Oliviero, L.; Bazin, P.; Daturi, M.; Costentin, G.; Maugé, F. How to determine IR molar absorption coefficients of co-adsorbed species? Application to methanol adsorption for quantification of MgO basic sites. *Phys. Chem. Chem. Phys*. **2011**, 13, 10797−10807.

(19) Stelmachowski, P.; Sirotin, S.; Bazin, P.; Maugé, F.; Travert, A. Speciation of adsorbed CO2 on metal oxides by a new 2-dimensional approach: 2D infrared inversion spectroscopy (2D IRIS). *Phys. Chem. Chem. Phys*. **2013**, 15, 9335−9342.

(20) El-Roz, M.; Bazin, P.; Birsa C□elic□, T.; Zabukovec Logar N.; Thibault-Starzyk, F. Pore Occupancy Changes Water/Ethanol Separation in a Metal–Organic Framework—Quantitative Map of Coadsorption by IR. *J. Phys. Chem. C.* **2015**, 119, 22570−22576.

(21) Vilmin, F.; Bazin, P.; Thibault-Starzyk F.; Travert, A. Speciation of adsorbates on surface of solids by infrared spectroscopy and chemometrics. *Analytica Chimica Acta*. **2015**, 891, 79-89.

(22) Dovesi, R.; Orlando, R.; Erba, A.; Zicovich-Wilson, C. M.; Civalleri, B.; Casassa, S.; Maschio, L.; Ferrabone, M.; De La Pierre, M.; D'Arco, P.; Noel, Y.; Causa, M.; Rerat, M.; Kirtman, B. CRYSTAL14: A program for the ab initio investigation of crystalline solids. *Int. J. Quantum Chem.* **2014**, *114*, 1287-1317.

(23) Peintinger, M. F.; Vilela Oliveira, D.; Bredow, T. Consistent Gaussian basis sets of triple-zeta valence with polarization quality for solid-state calculations. *J. Comput. Chem*. **2012**, *34*, 451.

(24) Peterson, K. A.; Figgen, D.; Goll, E.; Stoll, H.; Dolg, M. Systematically convergent basis sets with relativistic pseudopotentials. II. Small-core pseudopotentials and correlation consistent basis sets for the post-d group 16–18 elements. *J. Chem. Phys.* **2003**, *119*, 11113–11123.

(25) Piskunov, S.; Heifets, E.; Eglitis, R. I.; Borstel, G. Bulk properties and electronic structure of SrTiO3, BaTiO3, PbTiO3 perovskites: an ab initio HF/DFT study. *Comput. Mater. Sci.* **2004**, *29*, 165-178.

(26) Libowitzky, E. Correlation of O-H stretching frequencies and O-H…O hydrogen bond lengths in minerals. *Springer-Verlag Wien*. **1999**, *130* (8), 1047–1059.

(27) Emori, S.; Inoue, M.; Kishita, M.; Kubo, M. Magnetic properties of ammonium, sodium, and lithium pentafluoromanganates(III). *Inorg. Chem*. **1969**, *8* (7), 1385–1388.

(28) Barnes, A. D. J; Baikie, T.; Hardy, V.; Lepetit, M.-B.; Maignan, A.; Young, N. A.; Grazia Francesconi, M.; Magnetic coupling and long-range order in the spin–chain sulfide Ba_2CoS_3. *J. Mater. Chem.* **2006**, *16***,** 3489-3502

(29) Stout J. W. and Hadley, W. B. Heat Capacity of α- $NiSO_4 \cdot 6H_2O$ between 1 and 20°K. Electronic Energy Levels of the Ni^{++} Ion. *J. Chem. Phys*. **1964**, *40*, 55

(30) Weast, R. C., Ed. *CRC Handbook of Chemistry and Physics, 68th ed.; CRC Press Inc.: Boca Raton, FL*. **1987−1988**; p E-117.

(31) Viola, M. C.; Martínez-Lope, M. J.; Alonso, J. A.; Martínez, J. L.; De Paoli, J. M.; Pagola, S.; Pedregosa, J. C.; Fernández-Díaz, M. T.; Carbonio, R. E. Structure and Magnetic Properties of Sr_2CoWO_6: An Ordered Double Perovskite Containing Co2+(HS) with Unquenched Orbital Magnetic Moment. *Chem. Mater.* **2003**, *15*, 1655–1663

(32) Cox, D. E.; Shirane, G.; Frazer, B. C. Neutron- Diffraction Study of Antiferromagnetic Ba2CoWO6 and Ba_2NiWO_6. *J. Appl. Phys.* **1967**, *38*, 1459.

(33) Moreira, P. R.; F. Illas, A unified view of the theoretical description of magnetic coupling in molecular chemistry and solid-state physics. *Phys. Chem. Chem. Phys.* **2006**, 8, 1645-1752.

(34a) Sanz, F., Parada, C., Rojo, J.M., Ruíz-Valero, C., 2001. Synthesis, Structural Characterization, Magnetic Properties, and Ionic Conductivity of $Na_4M^{II}_3(PO_4)_2(P_2O_7)$ (M^{II} = Mn, Co, Ni). Chem. Mater. 13, 1334–1340.

(34b) Tang, Y., He, Z., Guo, W., Zhang, S., Yang, M., 2014. Syntheses and Magnetic Properties of New Tellurite–Sulfate Compounds $M_2(TeO_3)(SO_4)\cdot H_2O$ (M = Co, Mn) with a Layer Structure Showing a Distorted Honeycomb Spin–Lattice. Inorg. Chem. 53, 5862–5868.

(34c) Zhang, W.-L., He, Z.-Z., Xia, T.-L., Luo, Z.-Z., Zhang, H., Lin, C.-S., Cheng, W.-D., 2012. Syntheses and Magnetic Properties Study of Isostructural $BiM_2BP_2O_{10}$ (M = Co, Ni) Containing a Quasi-1D Linear Chain Structure. Inorg. Chem. 51, 8842–8847.

(34d) Herweijer, A., de Jonge, W.J.M., Botterman, A.C., Bongaarts, A.L.M., Cowen, J.A., 1972. Magnetic Studies of the Canted Ising Linear Chain CsCoCl-$2H_2O$. Phys. Rev. B 5, 4618–4630.